2013 IEEE International Conference on Robotics and Automation (ICRA)
Karlsruhe, Germany, May 6-10, 2013

Real-Time Reconstruction of Contact Shapes for Large Area Robot Skin

Luca Muscari[1], Lucia Seminara[2], Fulvio Mastrogiovanni[1],
Maurizio Valle[2], Marco Capurro[3] and Giorgio Cannata[1]

***Abstract*— Tactile sensing is considered a key technology for implementing complex robot interaction tasks. The contribution of this article is two-fold: (i) we propose a general-purpose algorithm for the reconstruction of deformation and force distributions for capacitance-based skin-like systems; (ii) real-time performance can be tuned according to available computational resources, which leads to an any-time formulation. Experiments (both in simulation and with real robot skin) provide a quantitative analysis of results.**

I. Introduction

During the past few years, the problem of the physical interaction through *touch* between robots and humans or the surrounding environment has received increasing attention in the literature [1], [2], [3], [4]. Much research work has been carried out to provide robots with the "sense of touch" [5], [6], [7]. To this aim, large-scale, whole-body robot *skin* is considered a key technology for implementing tactile-based robot interaction tasks.

A principled integration between interaction-oriented control frameworks and tactile representation structures is an important challenge: (i) it is necessary to provide control algorithms with information about the contact features (e.g., deformation and shape) in order to guide robot motions [8], [9], [10]; (ii) real-time performance must be guaranteed as far as the sensing architecture is concerned [11].

On the one hand, a number of approaches have been proposed to retrieve contact parameters out of tactile information. Image processing techniques are used in [12] to recognize objects manipulated by robotic hands. Fingertip tactile *images* are used to retrieve information about the contact condition, with the aim of determining incipient slip behaviours. Tactile information is used in [13], [14] to inform grasp closure, where multiple contact points are needed for a stable grasping. On the other hand, other approaches are devoted to recognize and classify specific shapes of objects in contact. The work of Liu *et al*. [15] is aimed at designing a computationally efficient algorithm for recognizing simple contact *shapes* through machine learning techniques. Unfortunately, the algorithm cannot be extended to generic shapes. Other features are considered in [16], such as mobility (i.e., an object is moving on the robot surface) and compliance (i.e., hard versus soft objects). Again, the proposed algorithm is only focused on recognizing specific features. Roughness is the feature of choice for the approach discussed in [17]. Drimus *et al*. [18] focus on the recognition of *deformable* objects through tactile sensors on fingertips. In a more general perspective, the reconstruction of generic contact shapes using Electrical Impedance Tomography (EIT) is discussed in [19]. Unfortunately, computational issues are not considered.

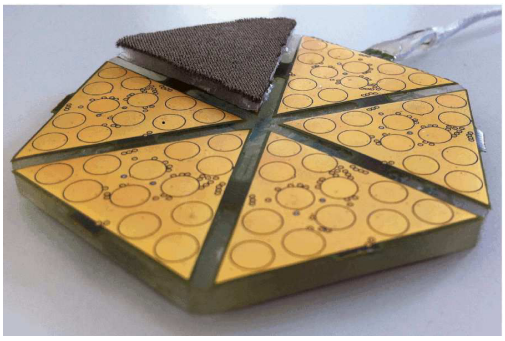

Fig. 1. A hexagonal patch made up of six triangular modules. One module is covered by the elastomer and the ground plane.

The contribution of this article is two-fold: (i) a general-purpose algorithm is proposed, which allows for the reconstruction of deformation and force distributions for capacitance-based skin-like systems; (ii) a real-time SW architecture that allows for tuning the algorithm performance according to available computational resources, which leads to an any-time formulation.

The article is organized as follows. Section II introduces the reference tactile technology and the basic principles. Section III describes the model and the associated implementation issues. Experiments (both in simulation and with real robot skin) are presented in Section IV. Conclusions follow.

II. Artificial Skin for Robots and Contact Mechanics

A. The Reference Robot Skin Technology

The considered *robot skin* technology has been described in [5], [7]. The adopted sensing mode refers to the capacitance-based transduction principle. The skin hosts a number of transducers (i.e., *taxels*) organized in a layered

The research leading to these results has received funding from the European Community's Seventh Framework Programme under Grant Agreement no. 231500 (ROBOSKIN).

[1]L. Muscari, F. Mastrogiovanni and G. Cannata are with the Department of Informatics, Bioengineering, Robotics and Systems Engineering, University of Genoa, Via Opera Pia 13, 16145, Genoa, Italy. Corresponding author's email: fulvio.mastrogiovanni@unige.it.

[2]L. Seminara and M. Valle are with the Department of Telecommunications, Electronic, Electric and Naval Engineering, University of Genoa, Via Opera Pia 13, 16145, Genoa, Italy.

[3]M. Capurro is with the Department of Civil, Chemical and Environmental Engineering, University of Genoa, P.le Kennedy 1, 16129, Genoa, Italy.

structure (Figure 1). The lower layer is made up of a number of spatially distributed taxels (i.e., circle pads acting as positive electrodes), which are geometrically organized in triangular modules of 3 cm side, each module comprising a 2D tactile sensing array as well as embedded and dedicated read-out electronics, i.e., a small Capacitance to Digital Converter (CDC) chip. The CDC chip can measure variations in capacitance values within the $4 \div 30$ pF range with a sensitivity of 0.32 pF. The upper layer is a ground electrode. Finally, the central layer is a soft elastomer acting as a dielectric between the two electrodes.

Normal forces exerted on the robot skin produce variations in capacitance values reflecting the varied pressure over taxels. In ideal conditions, the capacitance C associated with each taxel linearly depends on the dielectric constant ϵ_0, the relative permittivity of the dielectric material ϵ_r, the overlap area A and the distance h (i.e., the dielectric thickness) between the two electrodes:

$$C = \epsilon_0 \epsilon_r \frac{A}{h}. \tag{1}$$

Considering the capacitance model of (1), the output value of the CDC chip for each taxel corresponds to:

$$\hat{\sigma} = \Delta C = C_p - C_n = \epsilon_o \epsilon_r A \frac{h_n - h_p}{h_n h_p}, \tag{2}$$

where C_p and h_p are, respectively, the capacitance value and the elastomer thickness in the *contact* case, whereas C_n and h_n correspond to the *no contact* or nominal case. A pressure exerted on taxels produces an increment in capacitance according to (2).

Triangular modules are arranged in *patches*, which are surface-compliant structures covering large parts of a robot body. Each patch is associated with a microcontroller responsible to acquire and early process data from each triangular module. Each taxel is a 4 mm diameter transducer. Up to 12 taxels and the corresponding electronics are hosted on a triangular flexible Printed Circuit Board (fPCB). Up to 16 triangles can be managed by one microcontroller through four I^2C buses, which convey tactile information to the patch microcontroller. Each microcontroller is connected to a CAN bus line, so that the network of microcontrollers in *daisy chain* is connected to a master node (e.g., an embedded PC104 box) where higher level processing occurs [11]. The elastomer is the Ecoflex 00-30 silicone rubber commercialized by Smooth-On[1], which is characterized by interesting properties as will be discussed in Section III.

B. Principles of Contact Mechanics

Humans are able to reconstruct the shape of a given object in contact using information (in terms of stress and strain) originating from mechanoreceptors located in the skin [20], [21]. In Robotics, it is common to refer to the *Forward Elastic Problem* as the process of determining stress and strain components as a result of a contact, and to the *Inverse Elastic Problem* as the process of reconstructing the contact features (e.g., shape or exerted forces) from stress and strain measurements [22].

[1]Please refer to the Smooth-On website at http://www.smooth-on.com.

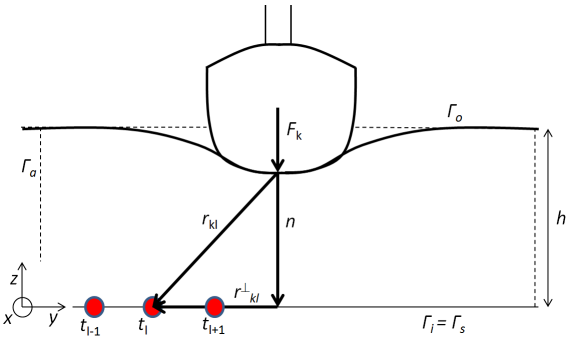

Fig. 2. A typical contact scenario.

Let us assume a 3D Cartesian frame (x, y, z), with z pointing outwards, as shown in Figure 2. Adopting the framework introduced in [23], let us assume that the part of the elastic layer (i.e., the elastomer) interested by the contact is a volume Σ comprised between an outer surface Γ_o (interested by the contact with the object), an inner surface Γ_i (mechanically coupled with a rigid surface, i.e., the robot body) and the faces Γ_a around the layer. The sensors (red circles in Figure 2) are assumed to be located on a plane Γ_s inside Σ, possibly coincident with Γ_i. We refer to the Cauchy stress tensor $\boldsymbol{\sigma}$ and in particular to:

$$\sigma_{ij}(x, y, z), \quad i, j \in \{x, y, z\}, \tag{3}$$

as the stress component on the plane (i, j) inside Σ at location (x, y, z). We refer also to the vector $\boldsymbol{u} \in \mathbb{R}^3$ and in particular to:

$$u_i(x, y, z), \quad i \in \{x, y, z\}, \tag{4}$$

as the displacement along the direction i at location (x, y, z). The stress component σ_{ii} represents a normal stress, σ_{ij}, with $i \neq j$, represents a shear stress and $\sigma_{ij} = \sigma_{ji}$ for each i and j. In such a framework, it is customary to assume that [22], [23]: (i) the elastic layer is isotropic, homogeneous and linear; (ii) a rigid plane Γ_i is present beneath; (iii) the interaction occurs in static conditions and perpendicular to the surface Γ_o; (iv) friction is negligible.

A Forward Elastic Problem consists in determining the distribution $\boldsymbol{\sigma}_s$ of the stress elements σ_{ij} on Γ_s given the distribution $\boldsymbol{u}_o$ of all the displacement elements u_i on the external surface Γ_o. The solution is obtained by solving [22]:

$$\nabla \cdot \boldsymbol{\sigma}_s = \mu \nabla^2 \boldsymbol{u} + (\lambda + \mu) \nabla (\nabla \cdot \boldsymbol{u}), \tag{5}$$

where μ and λ are the Lamè elastic moduli and $\boldsymbol{u}$ is the displacement field in Σ in absence of volume forces. When the contact area is smaller than Γ_o, it is possible to consider $\Gamma_o = \Gamma_{o,c} \cup \Gamma_{o,f}$, where $\Gamma_{o,c}$ represents the area in contact and $\Gamma_{o,f}$ represent the free but still deformed area. The boundary conditions for (5) are: $\boldsymbol{u} = 0$ on Γ_i, $\boldsymbol{u} = \boldsymbol{u}_{o,c}$ on $\Gamma_{o,c}$; $\boldsymbol{\sigma} \cdot \boldsymbol{n} = 0$ on $\Gamma_a \cap \Gamma_{o,f}$, where $\boldsymbol{n}$ is the vector normal to Γ_o.

Let us assume that each taxel t_l, located in $(x_l, y_l, 0)$ on $\Gamma_s = \Gamma_i$, can measure a stress value $\hat{\sigma}_{ij}(x_l, y_l, 0)$[2]. An Inverse Elastic Problem consists in retrieving the distribution $\boldsymbol{u}_o$ of all the deformation elements u_i on the external surface Γ_o given a discrete estimate $\hat{\boldsymbol{\sigma}}_s$, in the form of taxel measurements $\hat{\sigma}_{ij}$ of (2), of the distribution $\boldsymbol{\sigma}_s$ of the stress elements σ_{ij} on Γ_s.

According to [23], the Inverse Problem can be formalized as an optimal control problem. We assume a state variable $\boldsymbol{\sigma}_s$ (standing for the distribution of stress elements σ_{ij} in Γ_s) and a control signal $\boldsymbol{v}_o$ (standing for the deformation elements u_i in Γ_o), and we notice that the stress distribution $\boldsymbol{\sigma}_s$ can be modelled as a function of the control signal $\boldsymbol{v}_o$ (i.e., the deflections on Γ_o), namely $\boldsymbol{\sigma}_s = \boldsymbol{\sigma_s}(\boldsymbol{v}_o)$. Then the state equation reduces to (5), where the boundary conditions are: $\boldsymbol{u} = 0$ on Γ_i; $\boldsymbol{u} = \boldsymbol{v}_o$ on Γ_o; $\boldsymbol{\sigma} \cdot \boldsymbol{n} = 0$ on $\Gamma_a \cap \Gamma_{o,f}$. The optimal control formulation allows to retrieve the displacement vector $\boldsymbol{u}_o$ on Γ_o as the value of $\boldsymbol{v}_o$ minimizing the functional:

$$\int_{\Gamma_s} ||\boldsymbol{\sigma}_s(\boldsymbol{v}_o) - \hat{\boldsymbol{\sigma}}_s||^2 \, d\Gamma_s. \tag{6}$$

As it can be noticed, the formulation of (6) is Hadamard ill-posed.

III. Computation of Force and Deformation Distributions on Robot Skin

A. Retrieving the Distributions of Force and Deformation

In this Section, we derive a possible solution to the Inverse Elastic Problem introduced in Section II-B [24]. Let us assume that a set of taxels $T = \{t_1, \ldots, t_l, \ldots, t_L\}$ is available and located on $\Gamma_s = \Gamma_i$. Each taxel provides a measured stress value $\hat{\sigma}_l$. A mapping exists between the index l and the location $(x_l, y_l, 0)$ of the taxel t_l on Γ_s. Along with elastomer linearity, let us assume *small deformations* and a Poisson's coefficient $\nu = 0.5$ (which is a appropriate for the adopted elastomer). With reference to Figure 2, let us assume to divide the outer surface Γ_o in a grid of K locations. For each location k, with $k = 1, \ldots, K$, we define $\boldsymbol{F}_k$ as the force exerted on the elastomer in k and $\boldsymbol{F} = \{\boldsymbol{F}_1, \ldots, \boldsymbol{F}_k, \ldots, \boldsymbol{F}_K\}$ as the discrete force distribution. A mapping exists between the index k and the location (x_k, y_k, h) of the force $\boldsymbol{F}_k$ on Γ_o. Furthermore, we assume that $\boldsymbol{F}_k$ can be decomposed in a normal component $\boldsymbol{F}_k^n$ and a perpendicular component $\boldsymbol{F}_k^\perp$ to Γ_o.

We refer to $\boldsymbol{r}_{kl}$ as the distance vector between location k on Γ_o and taxel location l on Γ_s, as follows:

$$\boldsymbol{r}_{kl} = \boldsymbol{r}_{kl}^n + \boldsymbol{r}_{kl}^\perp, \tag{7}$$

where $\boldsymbol{r}_{kl}^n = \boldsymbol{n}h$ is the normal projection of k on Γ_s and $\boldsymbol{r}_{kl}^\perp$ is the distance between the projection of k on Γ_s and taxel location l. According to the Boussinesq equation [22], the stress tensor $\boldsymbol{\sigma}_l$ generated in t_l by the discrete force distribution $\boldsymbol{F}$ is:

$$\boldsymbol{\sigma}_l = \frac{3}{2\pi} \sum_{k=1}^{K} \frac{\boldsymbol{F}_k \cdot \boldsymbol{r}_{kl}}{r_{kl}^5} \boldsymbol{r}_{kl} \otimes \boldsymbol{r}_{kl}, \tag{8}$$

where $r_{kl} = (\boldsymbol{r}_{kl} \cdot \boldsymbol{r}_{kl})^{\frac{1}{2}}$. The summation is executed for each force contribution k of the discrete distribution. Since we consider only normal stresses, it is possible to reduce (8) to:

$$\boldsymbol{n} \cdot \boldsymbol{\sigma}_l = \frac{3}{2\pi} \sum_{k=1}^{K} \frac{\boldsymbol{F}_k \cdot \boldsymbol{r}_{kl} h}{({\boldsymbol{r}_{kl}^\perp}^2 + h^2)^{\frac{5}{2}}} \boldsymbol{r}_{kl}. \tag{9}$$

It is noteworthy that (9) must be solved for each taxel t_l. Since we have K force application points and L taxels providing measurements, (8) and (9) can be rewritten in matrix form:

$$\boldsymbol{\sigma}_s = C\boldsymbol{F}, \tag{10}$$

where $\boldsymbol{\sigma}_s \in \mathbb{R}^L$ is the stress distribution on Γ_s introduced in Section II-B, $\boldsymbol{F} \in \mathbb{R}^K$ is the force distribution on Γ_o and $C \in \mathbb{R}^{L \times K}$ is a matrix whose elements c_{lk} are:

$$\frac{3}{2\pi} \sum_{k=1}^{K} \frac{\boldsymbol{F}_k \cdot \boldsymbol{r}_{kl} h}{({\boldsymbol{r}_{kl}^\perp}^2 + h^2)^{\frac{5}{2}}} \boldsymbol{r}_{kl}. \tag{11}$$

In real-world applications, whilst the number of taxels L is typically given by the design of the sensing surface, the choice of K is arbitrary. It is obvious that, when $L = K$, the matrix C is full rank and invertible, which leads to:

$$\boldsymbol{F} = C^{-1}\boldsymbol{\sigma}_s. \tag{12}$$

As a consequence, given a set of taxel measurements $\hat{\boldsymbol{\sigma}}_s$, an estimate $\hat{\boldsymbol{F}}$ of the discrete force distribution $\boldsymbol{F}$ can be obtained using (12). It is legitimate to choose a grid on Σ_o such that $L \neq K$ when it is necessary to deal in real-time with the force distribution reconstruction. Section III-B further elaborates on this. In such a case, the C matrix is still invertible using, e.g., the Moore-Penrose psudoinverse, which leads to a generalized version of (12):

$$\boldsymbol{F} = C^{+}\boldsymbol{\sigma}_s. \tag{13}$$

It is noteworthy that C^+ is only one of the possible solutions to (13) and it may not be physically acceptable. However, it can be used to bootstrap a feasible solution [24]. Once the distribution of forces is known using (12) or (13), it is possible to compute the distribution of deformations $\boldsymbol{u}_o$ on Γ_o. If we consider a discrete area unit Δs_k corresponding to the location k where $\boldsymbol{F}_k$ is applied, we note that the elements c_{lk} of (11) are a discretization of the Green function on Γ_o, and (13) locally corresponds to:

$$\boldsymbol{F}_k = \boldsymbol{q}_k \Delta s_k, \tag{14}$$

where $\boldsymbol{q}_k$ is the 3D surface stress vector in k. The computation of displacements $\boldsymbol{u}_o$ produced by a distributed force $\boldsymbol{F}$ on a given surface area is computationally inefficient. On the contrary, surface deflections originating from the application of a set of forces concentrated on specific locations can

[2]The capacitance-based transduction principle only allows for detecting *strain* components along the normal direction. However, the stress-strain relationship can be obtained through a mechanical characterization of the elastic layer.

be efficiently computed. To this aim, given the linearity assumption, we use the Landau-Lifsitz solution of the elastic problem for a half-space [22]. The component tangential to the surface Γ_o is as follows:

$$\boldsymbol{u}_o^{\perp}(z,\boldsymbol{r}^{\perp}) = \frac{3}{4\pi \boldsymbol{r} E}\left\{\boldsymbol{F}^n\frac{\boldsymbol{r}^{\perp}z}{r^2} + \boldsymbol{F}^{\perp} + \boldsymbol{r}^{\perp}\boldsymbol{F}^{\perp}\cdot\boldsymbol{r}^{\perp}\frac{1}{r^2}\right\}, \tag{15}$$

where $\boldsymbol{r}^{\perp}$, $\boldsymbol{r}$, $\boldsymbol{F}^n$ and $\boldsymbol{F}^{\perp}$ indicate, respectively, generalized versions of $\boldsymbol{r}_{kl}^{\perp}$, $\boldsymbol{r}_{kl}$, $\boldsymbol{F}_k^n$ and $\boldsymbol{F}_k^{\perp}$ for any k and l, whereas E is the Young modulus of the elastomer. The normal component is given by:

$$\boldsymbol{u}_o^{n}(z,\boldsymbol{r}^{\perp}) = \frac{3}{4\pi \boldsymbol{r} E}\left\{\boldsymbol{F}^n\left(1+\frac{z^2}{r^2}\right) + \boldsymbol{r}^{\perp}\cdot\boldsymbol{F}^{\perp}\frac{z}{r^2}\right\}. \tag{16}$$

Displacements in Γ_o can be obtained using (15) and (16) imposing $z = 0$. Furthermore, in Γ_s (i.e., when $z = h$) displacements must be null. These conditions can be achieved by considering the *effective* surface displacement as:

$$\boldsymbol{\delta}_o = \boldsymbol{u}_o(z,0) - \boldsymbol{u}_o(z,h). \tag{17}$$

Using (17), it is possible to compute both tangential and normal displacements. If we consider the displacement at a given point l produced by the whole set $\boldsymbol{F}$ of concentrated forces, the tangential displacement in l is:

$$\begin{aligned}\boldsymbol{\delta}_{o,l}^{\perp} &= \frac{3}{4\pi E}\sum_{k=1}^{K}\frac{1}{\boldsymbol{r}_{kl}^{\perp}}\left\{\boldsymbol{F}_k^{\perp} + \frac{\boldsymbol{r}_{kl}^{\perp}\boldsymbol{F}_k^{\perp}\cdot\boldsymbol{r}_{kl}^{\perp}}{r_{kl}^2}\right\} \\ &- \frac{1}{\boldsymbol{r}_{kl}^{n}}\left\{\boldsymbol{F}_k^n\frac{\boldsymbol{r}_{kl}^n h}{r_{kl}^2} + \boldsymbol{F}_k^{\perp} + \frac{\boldsymbol{r}_{kl}^n\boldsymbol{F}_k^{\perp}\cdot\boldsymbol{r}_{kl}^n}{r_{kl}^2}\right\},\end{aligned} \tag{18}$$

whereas the normal displacement can be computed as:

$$\boldsymbol{\delta}_{o,l}^{n} = \frac{3}{4\pi E}\sum_{k=1}^{K}\frac{1}{r_{kl}}\left\{\boldsymbol{F}_k^n\left(1+\frac{h^2}{r_{kl}^2}\right) + \boldsymbol{r}_{kl}^{\perp}\cdot\boldsymbol{F}_k^{\perp}\frac{h}{r_{kl}^2}\right\}. \tag{19}$$

Unfortunately, displacements generated by a force $\boldsymbol{F}_k$ in a point l such that $l = k$ cannot be evaluated using (18) and (19) because $r_{ll} = 0$. In this case, the Boussinesq's solution can be used to retrieve an approximate evaluation. To this aim, we *pretend* that the elastomer has a thickness of $h + z_0$, where z_0 can be arbitrarily chosen to be sufficiently small. In particular, z_0 must be selected for each $k = l$ such that (14) holds. According to [22], this yields:

$$z_{0,k} = \left(\frac{3}{2\pi}\Delta s_k\right)^{\frac{1}{2}}. \tag{20}$$

If we apply the Work-Energy theorem, we have:

$$\boldsymbol{F}_k\cdot\boldsymbol{u}_{o,k} = \int_{\Sigma}\sigma:\epsilon \quad d\Sigma, \tag{21}$$

where ϵ is the stress tensor and : denotes the double tensor product. Analogously to the general case of (5), stress and strain are related by the elasticity equation that, in the assumption of linearity, is given by [22]:

$$\epsilon = \frac{1}{E}\left\{\boldsymbol{\sigma} - \nu\left(\mathbb{I}tr\boldsymbol{\sigma} - \boldsymbol{\sigma}\right)\right\}. \tag{22}$$

Substituting (22) in (21) we have:

$$\boldsymbol{F}_k\cdot\boldsymbol{u}_{o,k} = \frac{1}{E}\int_{\Sigma}(1+\nu)\,\boldsymbol{\sigma}:\boldsymbol{\sigma} - \nu tr^2\boldsymbol{\sigma} \quad d\Sigma. \tag{23}$$

Recalling (8) and assuming $\nu = 0.5$, we observe that $\boldsymbol{\sigma}$: $\boldsymbol{\sigma} = tr^2\boldsymbol{\sigma}$. As a consequence, (23) reduces to:

$$\boldsymbol{F}_k\cdot\boldsymbol{u}_{o,k} = \frac{1}{E}\int_{\Sigma}\boldsymbol{\sigma}:\boldsymbol{\sigma} \quad d\Sigma, \tag{24}$$

which can be evaluated adopting a cylindrical Cartesian frame $(\boldsymbol{r}_{kp}^{\perp},\phi,z)$ centered in $(x_k,y_k,h+z_0)$, where $\boldsymbol{r}_{kp}^{\perp}$ is the generic distance between the point of application of $\boldsymbol{F}_k$ and a generic point p, according to (7). Omitting the algebra, the evaluation of (24) leads to:

$$\boldsymbol{\delta}_{o,k}^{\perp} = \frac{9}{4\pi E}\frac{\boldsymbol{F}_k^{\perp}}{z_{0,h}}\Psi\left(\frac{h}{z_{0,h}}\right), \tag{25}$$

for the perpendicular components and to:

$$\boldsymbol{\delta}_{o,k}^{n} = \frac{9}{2\pi E}\frac{\boldsymbol{F}_k^{n}}{z_{0,h}}\Psi\left(\frac{h}{z_{0,h}}\right), \tag{26}$$

for the normal components. In (25) and (26), the function Ψ is a logarithmic non-dimensional function such that $\Psi \to 0.25$ as $h/z_{0,h} \to \infty$. Since $z_{0,h} \ll h$ in realistic situations, we assume $\Psi = 0.25$ in all the experiments. The deflections computed using (18), (19), (25) and (26) can be used to estimate the distribution of displacements $\boldsymbol{u}_o$ on the outer surface Γ_o.

B. Implementation for Different Grid Types

From a computational perspective, the approach discussed in Section III can be best implemented when taxels are arranged as a square grid, which does not hold in our case (Figure 1). It is necessary to specify a mapping between the location $(x_l,y_l,0)$ of a taxel t_l on Γ_s and a corresponding point r_n, with $n = 1,\ldots,N$, on a regular square grid. To this aim, we proceed as follows.

1) A Delaunay triangulation $\mathbb{D}_s$ is applied over the patch taxel arrangement on Γ_s. Each taxel location $(x_l,y_l,0)$ is a vertex of the triangulation.
2) A virtual regular square grid $\mathbb{R}_s$ is superimposed to $\mathbb{D}_s$. Each vertex $r_n \in \mathbb{R}_s$ is contained in one triangle of $\mathbb{D}_s$, which is identified by three taxel locations, namely t_{l_1}, t_{l_2} and t_{l_3}.
3) Each vertex $r_n \in \mathbb{R}_s$ is assigned with a *virtual* sensory reading $\hat{\sigma}_n$ obtained as the convex combination of the three sensory readings $\hat{\sigma}_{l_1}$, $\hat{\sigma}_{l_2}$ and $\hat{\sigma}_{l_3}$ of, respectively, the vertices t_{l_1}, t_{l_2} and t_{l_3} of the triangle of $\mathbb{D}_s$ containing r_n. The position $(x_n,y_n,0)$ of r_n is first expressed as the convex combination of the three surrounding taxels t_{l_1}, t_{l_2} and t_{l_3}, namely $r_n = \alpha t_{l_1} + \beta t_{l_2} + \gamma t_{l_3}$, where the three unknown coefficients α, β and γ must by found such that $\alpha+\beta+\gamma = 1$. Then, the virtual sensory reading $\hat{\sigma}_n$ can be obtained as $\hat{\sigma}_n = \alpha\hat{\sigma}_{l_1} + \beta\hat{\sigma}_{l_2} + \gamma\hat{\sigma}_{l_3}$. The N virtual sensory readings can be used to fed the procedure described in the previous Section from (7) onwards.

Different remarks can be made at this point: (i) the regular square grid $\mathbb{R}_s$ can have different resolutions according to specific computational capabilities and processing upper bounds, which allows for a versatile implementation on systems with differing computational capabilities; (ii) different robot body parts can use regular square grids of different resolutions at the same time; (iii) for a given robot body part, the resolution can vary over time, e.g., by switching *on the fly* to a more dense grid, in order to mimic a sort of tactile *focus of attention*; (iv) the square regular grid allows for the application of the procedure described in the previous Section to virtually any taxel arrangement, provided that the transduction mechanism is based on the capacitive principle.

IV. Experimental Evaluation

A. Experimental Set-up

The procedure described in Section III-A and Section III-B has been first prototyped using MATLAB and then implemented in C++ using the *Skinware* framework [11], a real-time SW architecture for the management of large-scale robot skin. The results discussed in this Section refer to the C++ implementation.

Both simulations and experiments with real robot skin patches have been performed. Simulations have been carried out to evaluate how the algorithm reconstructs known deformation and force distributions. In particular, COMSOL Multiphysics[3] has been used to compute the deformation distributions subject to imposed force distributions as a comparison with the results in simulation of the procedure. Experiments with real skin patches have been performed to investigate the algorithm properties to deal with noisy sensory data and to characterize its real-time capabilities. The experimental set-up is as follows. Three Cartesian positioners from Thorlabs[4] allow to horizontally translate the patch and to rotate it along the vertical axis. A force distribution of up to 3 N can be induced by a linear actuator mounted along the vertical axis. The tip of the linear actuator, which is provided with a load cell to measure the peak force on the area below, can be mechanically coupled with indenters of various shapes.

Five are the parameters that have been varied during the experimental campaign, namely the location of the indenter pressure (i.e., over a given taxel, between two taxels and between three taxels), the indenter shape (i.e., a 0.6 cm half-sphere, a 1.2 cm half-sphere, a $0.3cm$ cylinder and a $1.2cm$ cylinder), the value of the exerted pressure (i.e., from 0.2 N to 3 N), the pressure period length (i.e., from 3 s to 7 s) and the grid resolution K (i.e., from $K = 100$ for a 10×10 grid to $K = 1600$ for a 40×40 grid). Each trial involving any combination of these parameters has been repeated 50 times for statistical significance.

B. Simulations

When testing a force and deformation reconstruction algorithm from a computational perspective, simulations are useful in order to evaluate the quality of the reconstruction starting from a *completely known* applied pressure distribution. Figure 3 on the left shows a triangulated hexagonal patch with $L = 72$ taxels, where the three taxels marked in red are loaded with a deformation of 0.2 mm, with the aim of simulating a *gentle touch*.

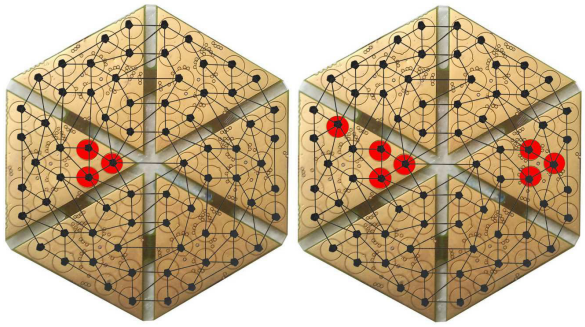

Fig. 3. Simulations. Left: a deformation of 0.2 mm is imposed to three red taxels. Right: the same deformation is imposed to three distinct contact points.

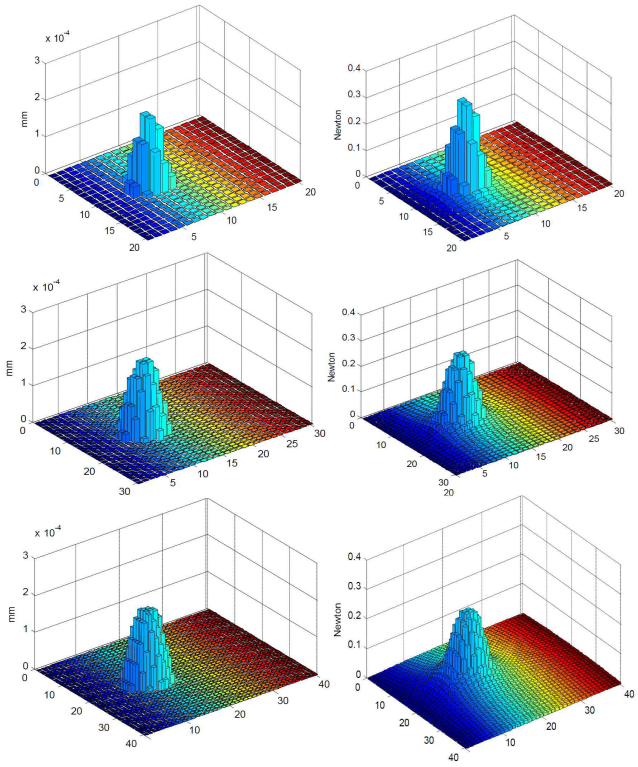

Fig. 4. Simulations. Reconstruction of the deformation (left column) and force (right column) distributions for 20×20, 30×30 and 40×40 grids (from top to bottom row) for the single contact case.

Figure 4 shows the results of the algorithm on grids of different resolutions when reconstructing deformation and force distributions for the imposed deformation of Figure 3 on the left. As it can be noticed, the peak of the deformation is correctly reconstructed around 0.2 mm. When considering the reconstruction of the force distribution, a smoothing

[3]Please refer to the COMSOL webpage at http://www.comsol.com.
[4]Please refer to the Thorlabs webpage at http://www.thorlabs.com.

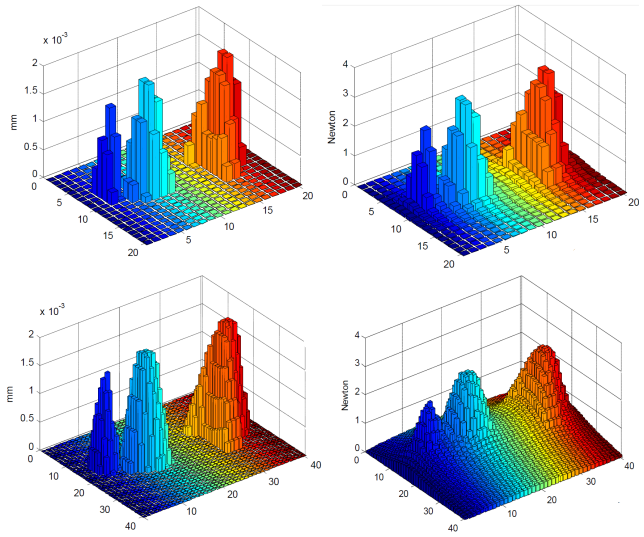

Fig. 5. Simulations. Reconstruction of the deformation (left column) and force (right column) distributions for 20×20 and 40×40 grids (from top to bottom row) for the multi contact case.

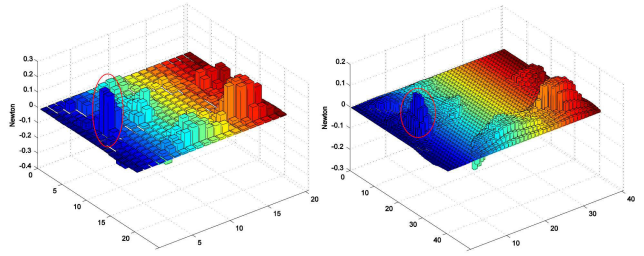

Fig. 6. Experiments. Examples of reconstruction of the force distribution over a single taxel for a $0.2\ N$ peak pressure, a 20×20 (left) and 40×40 (right) grid and a $1.2\ cm$ half-sphere indenter: the contact (red circle) cannot be isolated from noise.

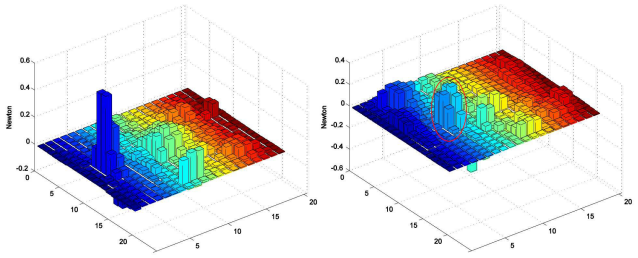

Fig. 7. Experiments. Examples of reconstruction of the force distribution over a single taxel (left) and in between three taxels (right) for a $0.5\ N$ peak pressure, a 20×20 grid and a $1.2\ cm$ half-sphere indenter: the contact becomes distinct from the noise.

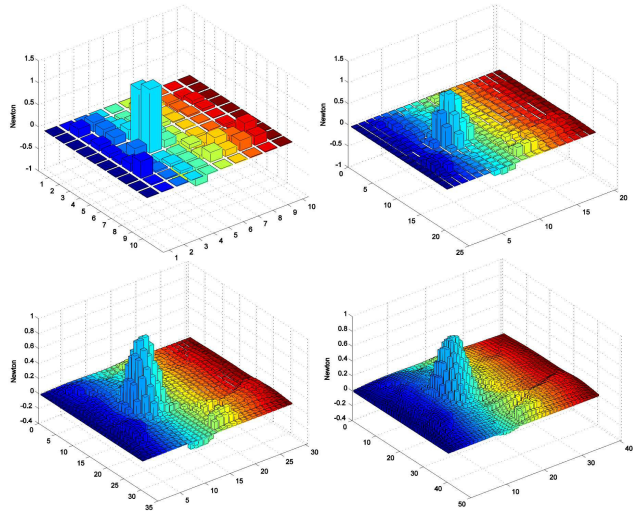

Fig. 8. Experiments. Examples of reconstruction of the force distribution in between three taxels for a $1.8\ N$ peak pressure, a 10×10 (top left), a 20×20 (top right), a 30×30 (bottom left) and a a 40×40 (bottom right) grid and a $1.2\ cm$ half-sphere indenter.

effect (which is more evident as long as the density of the grid is increased) can be observed which reproduces the typical visco-elastic behavior of the elastomer.

A multi-touch contact has been simulated where three distinct deformations of $0.2\ mm$ are applied to the patch (Figure 3 on the right). Figure 5 shows the results of the reconstruction of the deformation and force distributions in the multi-touch case. Also in this case, the three peaks are correctly centred around $0.2\ mm$. In spite of the observed smoothing effect, it is still possible to identify three distinct contact points.

C. Experiments with Real Robot Skin Patches

Figure 6 shows two examples of force reconstruction when a peak pressure of $0.2\ N$ is applied to a single taxel by a half-sphere. Independently from the grid resolution, the contact location cannot be isolated from noise. The situation can be improved by filtering raw tactile data before the algorithm is actually executed. However, the detection of contacts of $0.2\ N$ magnitude is not reliable.

Figure 7 shows two examples of force reconstruction when a peak pressure of $0.5\ N$ is applied to a single taxel (left) and in between of three taxels (right) by a $1.2\ cm$ half-sphere. With this pressure it is possible to distinguish the contact from the underlying raw data noise. In Figure 7 on the left it is possible to clearly distinguish the contact location, whereas in Figure 7 on the right the reconstruction is less clear, but still identifiable.

An example of the different resolutions that can be achieved given the same stimulus is shown in Figure 8. It can be noticed that as long as the resolution increases, the reconstructed surface is smoother. It may be argued that using a 40×40 grid resolution is pointless when using only 72 taxels. Indeed, this is an example of oversampling. However, the reconstruction faithfully – yet qualitatively – mimics the behavior of the elastomer, which can be useful for implementing fine grained contact shape recognition algorithms.

D. Performance

A number of tests have been performed to assess the overall performance of the algorithm as far as real-time performance is concerned. In particular, we decided to mediate

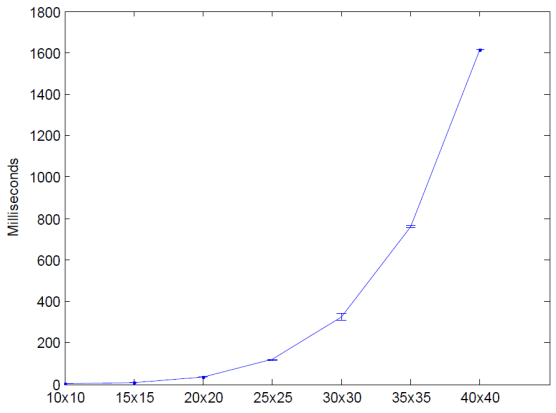

Fig. 9. Statistical time performance of the whole algorithm classified on the basis of the grid resolution K.

all the experiments we performed (with varying parameters) classifying them according to the grid resolution (i.e., the K parameter).

As it is shown in Figure 9, the temporal trend is exponential on the grid resolution. However, it is noteworthy that the standard deviations associated with computational times are almost negligible. This property is particularly important in real-time systems, where determinism is a *must have* feature. It is worth mentioning also that the majority of computational time is devoted to the matrix inversion of (12) and (13). As an example, the time needed to perform the remainder part of the algorithm in the 20×20 case is below $0.4\ ms$, whereas in the 40×40 case is around $1.4\ ms$.

V. Conclusions

In this article a general-purpose algorithm for the reconstruction of contact shapes and force distributions on capacitive sensor arrays has been presented and discussed. Both simulations and preliminary experiments with robot skin patches show the potentialities of the proposed approach. An analysis of the algorithm computational performance has been carried out, which can be used as reference to tune real-time performance on the basis of available resources at run-time.

References

[1] V. Lumelsky, *Sensing, intelligence, motion: How robots and humans move in an unstructured world*. New York, USA: Wiley and Sons, 2006.

[2] T. Taichi, , M. Takahiro, H. Ishiguro, and N. Hagita, "Automatic categorization of haptic interactions - what are the typical haptic interactions between a human and a robot?" in *Proceedings of the 2006 IEEE-RAS International Conference on Humanoid Robots (Humanoids 2006)*, Genoa, Italy, December 2006.

[3] B. Argall and A. Billard, "A survey of tactile human-robot interactions," *Robotics and Autonomous Systems*, vol. 58, no. 10, pp. 1159–1176, 2010.

[4] R. Dahiya, G. Metta, M. Valle, and G. Sandini, "Tactile sensing - from humans to humanoids," *IEEE Transactions on Robotics*, vol. 26, no. 1, pp. 1–20, 2010.

[5] G. Cannata, M. Maggiali, G. Metta, and G. Sandini, "An embedded artificial skin for humanoid robots," in *Proceedings of the 2008 IEEE International Conference on Multi-sensor Fusion and Integration (MFI'08)*, Seoul, Korea, August 2008.

[6] P. Mittendorfer and G. Cheng, "Humanoid multi-modal tactile sensing modules," *IEEE Transactions on Robotics*, vol. 27, no. 3, pp. 401–410, 2011.

[7] A. Schmitz, P. Maiolino, M. Maggiali, L. Natale, G. Cannata, and G. Metta, "Methods and technologies for the implementation of large-scale robot tactile sensors," *IEEE Transactions on Robotics*, vol. 27, no. 3, pp. 389–400, 2011.

[8] G. Cannata, S. Denei, and F. Mastrogiovanni, "Contact based robot control through tactile maps," in *Proceedings of the 2010 IEEE International Conference on Decision and Control (CDC'10)*, Atlanta, GA, USA, December 2010.

[9] P. Mittendorfer and G. Cheng, "Self-organizing sensory-motor map for low-level touch reactions," in *Proceedings of the 2011 IEEE-RAS International Conference on Humanoid Robotics (Humanoids 2011)*, Bled, Slovenia, October 2011.

[10] A. D. Prete, S. Denei, L. Natale, F. Mastrogiovanni, F. Nori, G. Cannata, and G. Metta, "Skin spatial calibration using force-torque measurements?" in *Proceedings of the 2011 IEEE-RSJ International Conference on Intelligent Robots and Systems (IROS 2011)*, San Francisco, CA, USA, October 2011.

[11] S. Youssefi, S. Denei, F. Mastrogiovanni, and G. Cannata, "A middleware for whole-body skin-like tactile systems," in *Proceedings of the 2011 IEEE-RAS International Conference on Humanoid Robotics (Humanoids 2011)*, Bled, Slovenia, October 2011.

[12] V. Ho, S. Hirai, A. Noda, and T. Nagatani, "What can be inferred from a tactile arrayed sensor in autonomous in-hand manipulation?" in *Proceedings of the 2011 IEEE International Conference on Automation Science and Engineering (CASE 2012)*, Seoul, Korea, August 2012.

[13] R. Krug, D. Dimitrov, K. Charusta, and B. Iliev, "Prioritized independent contact regions for form clusure grasps," in *Proceedings of the 2012 IEEE International Conference on Robotics and Automation (ICRA 2012)*, St. Paul, MN, USA, May 2012.

[14] K. Charusta, R. Krug, T. Stoyanov, D. Dimitrov, and B. Iliev, "Generation of independent contact regions on objects reconstructed from noisy real-world range data," in *Proceedings of the 2012 IEEE International Conference on Robotics and Automation (ICRA 2012)*, St. Paul, MN, USA, May 2012.

[15] H. Liu, X. Song, T. Nanayakkara, L. Seneviratne, and K. Althoefer, "A computationally fast algorithm for local contact shape and pose classification using a tactile array sensor," in *Proceedings of the 2012 IEEE International Conference on Robotics and Automation (ICRA 2012)*, St. Paul, MN, USA, May 2012.

[16] T. Bhattacharjee, J. Rehg, and C. Kemp, "Haptic classication and recognition of objects using a tactile sensing forearm," in *Proceedings of the 2012 IEEE-RSJ International Conference on Intelligent Robots and Systems (IROS 2012)*, Vilamoura, Portugal, October 2012.

[17] A. Petrovskaya and O. Khatib, "Global localization of objects via touch," *IEEE Transactions on Robotics*, vol. 27, no. 3, pp. 569–585, 2011.

[18] A. Drimus, G. Kootstra, A. Bilberg, and D. Kragic, "Classication of rigid and deformable objects using a novel tactile sensor," in *Proceedings of the 2011 IEEE International Conference on Advanced Robotics (ICAR 2011)*, Tallin, Estonia, June 2011.

[19] D. Tawil, D. Rye, and M. Velonaki, "Improved image reconstruction for an eit-based sensitive skin with multiple internal electrodes," *IEEE Transactions on Robotics*, vol. 27, no. 3, pp. 425–435, 2011.

[20] E. Kandel, J. Schwartz, and T. Jessell, *Principles of Neural Science (Fourth edition)*. New York, USA: McGraw-Hill, 2000.

[21] A. Serino and P. Haggard, "Touch and the body," *Neuroscience and Behavioral Reviews*, vol. 34, pp. 224–236, 2010.

[22] K. Johnson, *Contact Mechanics*. Cambridge, UK: Cambridge University Press, 1985.

[23] A. Caiti, G. Canepa, D. D. Rossi, F. Germagnoli, G. Magenes, and T. Parisini, "Towards the realization of an artificial tactile system: fine form discrimination by a tensorial tactile sensor array and neural inversion algorithms," *IEEE Transactions on Systems, Man and Cybernetics*, vol. 25, no. 6, pp. 933–946, 1995.

[24] L. Seminara, M. Capurro, A. Leoncini, and M. Valle, "Tactile data processing algorithms for the reconstruction of contact force distributions," *IEEE Transactions on Robotics (submitted)*.